Ultrasound-Guided Robot for Flexible Needle Steering

Article *in* IEEE Transactions on Biomedical Engineering · May 2010

DOI: 10.1109/TBME.2009.2030169 · Source: IEEE Xplore

2 authors, including:

Moshe Shoham
Technion - Israel Institute of Technology
164 PUBLICATIONS **2,988** CITATIONS

SEE PROFILE

Ultrasound-Guided Robot for Flexible Needle Steering

Zipi Neubach* and Moshe Shoham, *Associate Member, IEEE*

***Abstract*—The success rate of medical procedures involving needle insertion is often directly related to needle placement accuracy. Due to inherent limitations of commonly used freehand needle placement techniques, there is a need for a system providing for controlled needle steering for procedures that demand high positional accuracy. This paper describes a robotic system developed for flexible needle steering inside soft tissues under real-time ultrasound imaging. An inverse kinematics algorithm based on a virtual spring model is applied to calculate needle base manipulations required for the tip to follow a curved trajectory while avoiding physiological obstacles. The needle tip position is derived from ultrasound images and is used in calculations to minimize the tracking error, enabling a closed-loop needle insertion. In addition, as tissue stiffness is a necessary input to the control algorithm, a novel method to classify tissue stiffness from localized tissue displacements is proposed and shown to successfully distinguish between soft and stiff tissue. The system performance was experimentally verified by robotic manipulation of the needle base inside a phantom with layers of varying stiffnesses. The closed-loop experiment with updated tissue stiffness parameters demonstrated a needle-tip tracking error of $\sim$1 mm and proved to be significantly more accurate than the freehand method.**

***Index Terms*—Needle imaging, needle steering, robots, tissue stiffness, ultrasound.**

I. Introduction

NUMEROUS clinical procedures, including biopsies, local anesthesia, blood sampling, prostate brachytherapy, and ablation, require needle insertion for diagnostic or therapeutic purposes. To enable accurate needle placement with stress on appropriate placement of the needle tip into an organ, vessel, or lesion of interest, such insertions require precise navigation techniques. The accuracy of needle insertion can significantly influence the validity of a diagnostic procedure or the success rate of therapeutic treatments. More specifically, brachytherapy protocols, employing specially designed needles for directed delivery of radioactive seeds into tumors, have shown a direct correlation between treatment effectiveness and accuracy of needle placement [1]. Similarly, needle misplacement in needle aspiration biopsies can lead to misdiagnosis and loss of critical therapy time [2].

Manuscript received January 14, 2009; revised April 28, 2009 and June 29, 2009. First published August 25, 2009; current version published March 24, 2010. *Asterisk indicates corresponding author.*

*Z. Neubach is with the Robotics Laboratory, Department of Mechanical Engineering, Technion-Israel Institute of Technology, Haifa 32000, Israel (e-mail: zipiya@gmail.com).

M. Shoham is with the Robotics Laboratory, Department of Mechanical Engineering, Technion-Israel Institute of Technology, Haifa 32000, Israel (e-mail: shoham@tx.technion.ac.il).

Color versions of one or more of the figures in this paper are available online at http://ieeexplore.ieee.org.

Digital Object Identifier 10.1109/TBME.2009.2030169

Physicians often perform needle insertion procedures freehand, implementing force feedback methods for needle advancement along with and their 3-D perception of the anatomic structure. The precision of such procedures is limited and involves a steep learning curve. Although imaging techniques can improve target visibility and needle placement accuracy, target movement and needle deflection due to tissue deformation can still hinder absolute placement precision. Variability of soft tissue properties creates unpredictable discrepancies between the planning and treatment phases. A follow-up study of computed tomography (CT)-guided needle biopsies demonstrated that 14% of the tests proved futile due to needle misplacement [2]. Therefore, biopsy procedures are often repeated to ensure adequate sampling, exposing the patient to additional risks and potential complications.

Robotic guidance systems have been reported in applications designed to improve needle insertion accuracy in various biomedical procedures. Exercise of such navigation techniques has been demonstrated in several studies in directing needle orientation before manual or automatic insertion [3]–[8], model tissue deformation due to needle insertion [9], [10], and needle insertion forces [10], [11] and has even been proposed as a means of needle steering and path planning [12], [13]. However, to the best of our knowledge, no studies to date have applied ultrasound imaging for real-time steering of robotics-guided flexible needle insertion. A device featuring ultrasound-based guidance in place of X ray would offer a significant cut in imaging costs and radiation exposure when compared to CT and MRI and allow for increased mobility through its more compact design. Addition of ultrasound imaging options would provide for soft tissue imaging, blood velocity measurements, and flow imaging. Furthermore, real-time ultrasound-based imaging can be easily captured at any probe position or orientation.

Herein, we describe design of an ultrasound-imaging platform for real-time guidance of robotics-controlled flexible needle insertion as an upgraded version of the needle-steering device developed by Glozman and Shoham [14], which relied on real-time fluoroscopic imaging-based guidance. The system proposed in this study executes an automatic flexible needle insertion procedure based on a needle–tissue interaction model [14]. The device includes a robot designed to drive the needle tip in a predetermined, curved trajectory by maneuvering the needle base, while considering natural obstacles such as blood vessels, bones, and organs in the path planning. Moreover, image-processing algorithms were incorporated to continuously detect the needle tip position, enabling a closed-loop system for controlled needle insertion.

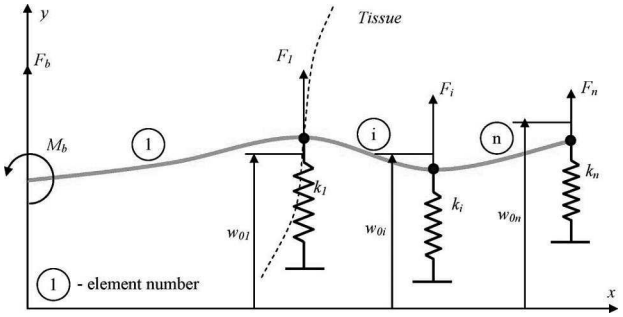

Fig. 1. Virtual spring model. This model views the needle as a segmented linear beam subjected to spring forces.

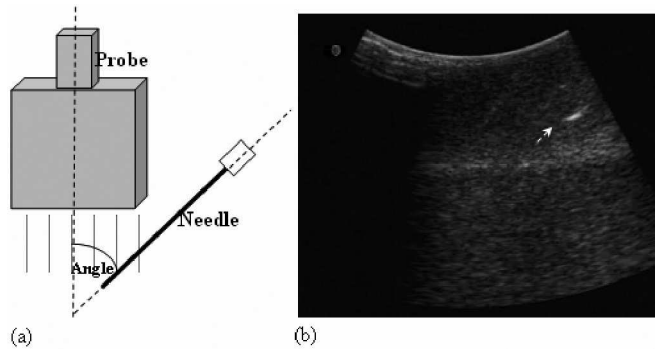

Fig. 2. (a) Needle-probe angle determining needle visibility. (b) Needle tip appearance in the ultrasound image in a 30° needle-probe setup (arrow).

II. Methods

A. Needle-Steering Model and Path Planning

The theoretical model for flexible needle steering in soft tissue is based on the virtual spring model presented in [14]. In this model, the needle is regarded as a linear beam divided into segments. Assuming small lateral needle displacements, the tissue response can be considered linear and the tissue forces are modeled by lateral virtual springs distributed along the needle. Hence, each segment is subjected to point forces F_i, which depend on both the local displacement w_i from the initial position w_{oi} and the tissue stiffness described by the virtual spring coefficient k_i (see Fig. 1).

From the boundary condition at the needle base, second-order continuity conditions and spring forces applied between elements, $4xn$ equations can be derived, where *n* is the number of elements and described by the following matrix expression:

$$KN = Q \tag{1}$$

where K is the matrix coefficients of N_{ij}, N is a vector of translation and slope at the edges of each element N_{ij}, where i is the element number and j is the degree of freedom at element i. Q is a vector including combination of stiffness coefficient and initial positions of the nodes at the times of their penetration with the needle.

Equation (1) can then be solved to calculate the needle base rotation and translation required for the needle tip to follow the desired path. This is the inverse kinematics problem solution. However, in this setting an infinite number of inverse kinematics solutions exist, each with its unique needle base position and orientation control inputs, all of which will eventually lead the needle tip along the same path. This issue was raised in previous works [14] and was solved as an optimization problem that calculated the control inputs while minimizing lateral pressure on the tissue.

B. Needle Visibility in Ultrasound Image

Needle visibility in the ultrasound image is mostly influenced by the operator's skill in aligning the needle within the imaging plane of the ultrasound probe [15]. Although we assume that the needle tip remains in the ultrasound probe's plane throughout the insertion path, the algorithm for steering developed here is equally valid for out-of-plane motion when 3-D ultrasound probes are utilized. Since the needle motion along the path is within the imaging plane, a registration procedure using a digitizer was performed for aligning the needle with the plane of the ultrasound probe. A digitizer is a mechanical device that measures a point's coordinates in space with respect to a defined coordinate system. The digitizer, first calibrated according to the robot's coordinate system, was used to position the center of the probe's width (imaging plane) in the needle's plane.

Needle visibility is also influenced by the angle between the needle and the central axis of the ultrasound probe [see Fig. 2(a)]. Experimentations with various angles demonstrated that the needle shaft but not the needle tip, is clearly visible in a 90° angle setup. However, at angles of 10°–30° the needle tip is clearly discernable, appearing as a bright area advancing with needle movement [see Fig. 2(b)]. In addition, these favorable angles are those, which are typically used in the clinics [16], [17] due to anatomical restrictions and were therefore used in our experiments.

C. Algorithm for Needle Tip Detection

Needle tip detection via ultrasound imaging is essential for a closed-loop needle-steering procedure and can be achieved as described in the following. As the needle tip advances, the main differences between consecutive image frames lie is the needle tip position. Such movements can then be detected by simple image subtraction of consecutive frames. In order to reduce background noise and effects of tissue deformation, only the immediate area around the needle tip is analyzed [see Fig. 3(a)]. Initially, this area is defined by the expected entry point, which is determined by the robot–ultrasound probe location. The area in the next frames is defined around the previously detected tip positions. A threshold is then applied on the cropped difference image [see Fig. 3(b)] and the center of mass of the largest bright area above that threshold is defined as the detected needle tip position [see Fig. 3(c)]. The final detected tip position is demonstrated in Fig. 3(d), which also was verified by direct measurements as follows.

In order to be able to match each pixel from the image coordinate system to the robot coordinate system, image to probe registration was applied based on [18], and probe to robot

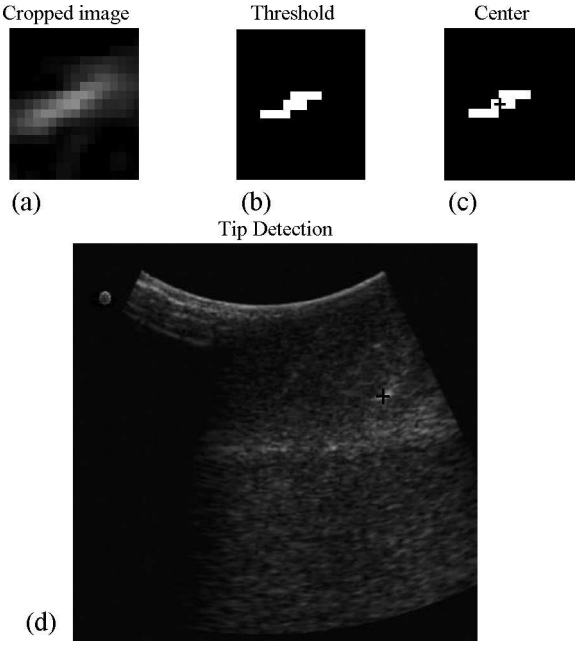

Fig. 3. Needle tip detection using ultrasound imaging. (a) Cropped image around the detected tip. (b) Image after threshold application to the image. (c) Needle tip is defined as the center of white area (black cross). (d) Original ultrasound image with detected needle tip (black cross).

transformation was measured using a digitizer. Using this image-robot registration, the detected needle tip position in the image was expressed in the robot's coordinate system and compared with the known position of the robot. The results of 16 experiments with various needle positions show mean error of 0.85 mm along the axial axis and 0.36 mm in the lateral axis. These results indicate that the bright area seen in the image is indeed the needle tip.

D. Tissue Stiffness Classification

The virtual spring model, which is necessary to calculate the required needle base movements, depends on the tissue stiffness coefficients. As the needle may encounter different tissue types during the insertion procedure, a method for online tissue stiffness classification must be included in the motion algorithm. Incorporation of such a method results in an improved needle-tracking performance, as detailed in Section III.

In the present investigation, a novel method for tissue stiffness classification is proposed as determined by local tissue motion in the area most anterior to the needle tip. Various reports describe tissue motion estimations, or elastography, particularly via ultrasound imaging [19]–[21]. As many pathological changes can be correlated with tissue stiffness modifications, early elastographic analyses were initiated for diagnosis of cancer. Recently, a similar tissue displacement estimation extrapolated from ultrasound images during needle insertion was suggested [22]. In this model, only axial rigid displacements were estimated and elastic properties were calculated by adjusting the measured displacements to the simulated ones. However, in the present research, elastic tissue properties are determined by 2-D, nonrigid displacements estimated in the region anterior to the needle tip, without the need for simulation, and can be used in any needle trajectory. The technique is based on the speckle-tracking algorithm and is detailed in the next section.

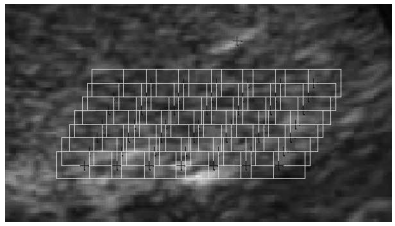

Fig. 4. Deviation of the area anterior to the needle tip position (upper black cross). The reference frame is divided into overlapping ROI (white rectangular) around the defined nodes (black crosses) placed in front of the needle tip (black cross).

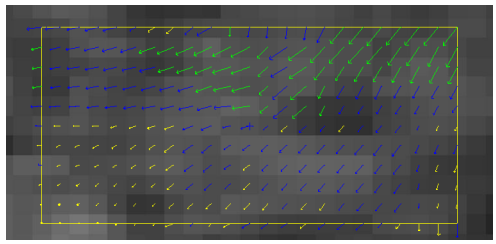

Fig. 5. Representative displacement results for all pixels in one block.

1) Block-Matching Algorithm: The elastography algorithm applied in the present study is based on the method presented in [21]. As the original method analyzed compression force-induced tissue motion, some modifications were made to adapt this method tissue motion analysis in the region anterior to the needle tip. Elastography is designed to estimate changes in tissue motion as determined by comparing the predeformation reference frame to the postdeformation comparison frame. First, the reference frame is divided into regions of interest (ROI) around the defined nodes, which are placed in front of the needle tip (see Fig. 4).

Based on the previously described model, [21] the ROI area was defined as twice the lateral and axial image resolution. Thus, application of a 3.5-MHz central frequency probe defined ROI parameters as 2.2 mm on the axial axis and 5.6 mm on the lateral axis. Furthermore, definition of overlapping ROIs increases displacement estimation accuracy [21]. Therefore, ROIs were arranged with a 60% and 50% overlap in their lateral and axial axes, respectively. Translation of the corners of each ROI was then calculated by a single-level block-matching algorithm [20]. The block-matching criterion is determined by minimizing the sum-of-squared difference. Pixel displacement within the ROI is then calculated based on a bilinear model, where the unknown parameters can be determined from the calculated displacement of the ROI corners [21]. Fig. 5 demonstrates a final motion estimation for one block between two imaging frames in which the needle advanced 1.5 mm.

2) Algorithm Verification: The speckle-tracking algorithm performance was verified by simulating an ultrasound image of known displacement, using the "Field 2" freeware [23]–[25], which enables ultrasound image simulations. An image of a

TABLE I
BLOCK-MATCHING ALGORITHM PERFORMANCE, MEAN ERRORS ± AND STD.

	Axial	Lateral
Lateral Translation	0 ± 0.01 [mm]	0.04 ± 0.03 [mm]
Lateral and axial deformation	0.01 ± 0 [mm]	0 ± 0.04 [mm]

linear transducer with 3.5-MHz central frequency and 64 elements was simulated, with and without deformation of a known degree. The speckle-tracking algorithm was then applied to the images for deformation estimations. The estimated displacement of each pixel was subtracted from the known displacement for calculation of the estimation error. A simple 0.5-mm lateral translation and a more complex axial deformation from -0.5 to 0 mm coupled with a lateral deformation from -0.3 to 0.3 mm were examined using this setup. The mean of absolute error results for all pixels (order of hundreds of thousands) and their standard deviation (std) are summarized in Table I. The error results indicate high performance of the speckle-tracking algorithm.

3) Simulations and Experiments Results for Tissue Motion: The contribution of tissue motion to tissue classification was further analyzed by simulations and experiments of needle insertion into both soft and stiff materials. Soft (10.5 kPa) and stiff (39.4 kPa) Dermasol with TiO2 phantoms were applied [26] to allow for a close mimic of the imaging characteristics and mechanical properties of human tissue. In addition, needle forces exerted on the materials were measured by a 6-DOF force sensor embedded within the robot structure. Needle forces can be modeled by the friction force uniformly distributed along the needle shaft and a pick force at the needle tip, which is considered the cutting force [9], [27]. The friction force per unit length is derived from the slope of the force after the main puncture is made [27], whereas the cutting force is estimated at the main puncture event detected by a sudden drop in force. The results for the friction forces obtained in our setup were 0.06 and 0.15 N/mm for soft and stiff dermasol, respectively, with cutting forces of 0.6 N for soft and 1 N for stiff dermasol, respectively.

a) One layer—simulations: One layer cross section (70 mm × 70 mm) of the dermasol phantom during insertion process were simulated using the structural mechanics module of the COMSOL Multiphysics Software. A needle of 1 mm width and a length equal to the insertion depth was simulated with fixed boundary conditions, with exception of the entry edge. The resulting displacement anterior to the needle tip as a function of distance for different needle depths is shown in Fig. 6.

The simulation shows that the displacement in front of the needle is larger in soft tissue than in stiff tissue, and that the tissue types can be distinguished according to tissue motion.

b) One layer—experiments: Representative results of tissue displacement in actual straight-line needle insertion in stiff and soft dermasol are shown in Fig. 7. The mean displacements determined for six experiments, which included about 10–15 frame pairs each are presented in Fig. 8. Experimental and simulation results matched, showing a larger degree of displacement upon needle insertion into soft tissue.

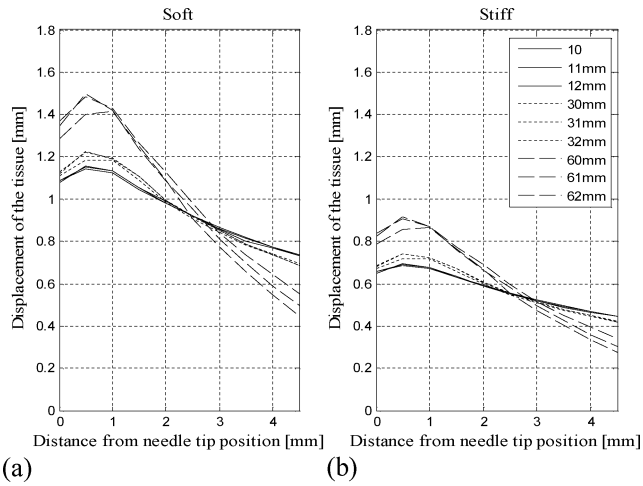

Fig. 6. Simulation results of tissue displacement anterior to the needle tip as function of distance from the needle tip position. Results are shown at varying depths of needle insertion as determined between two frames in which the needle advanced 0.5 mm for (a) soft tissue phantom and (b) stiff tissue phantom.

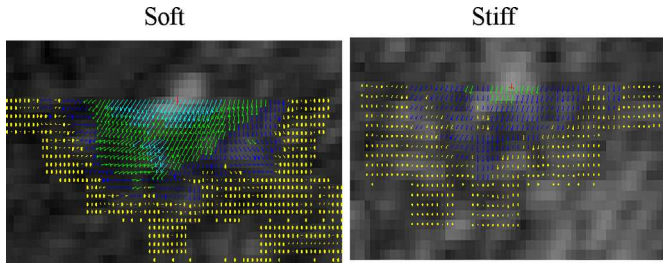

Fig. 7. Tissue displacement estimation of the area anterior to the needle tip inserted into soft or stiff materials. The displacement of each pixel is shown by an arrow, where the color of the arrow indicates the displacement magnitude: white <0.1 mm, black 0.1–0.2 mm, gray >0.4 mm.

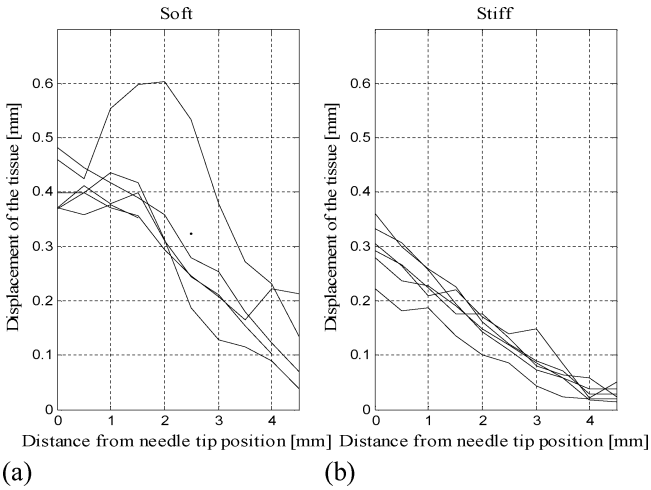

Fig. 8. Tissue displacement estimation of the area anterior to the needle tip in six independent experiments of straight-line needle insertions in (a) soft dermasol and (b) stiff dermasol.

c) Two layers—simulations: Simulations were then repeated with two layers of varying phantom stiffness at different needle locations, and the displacements of the areas anterior to the needle tip were analyzed. Similar to the results obtained from the simulations on one-layer phantom, the two-layer model with

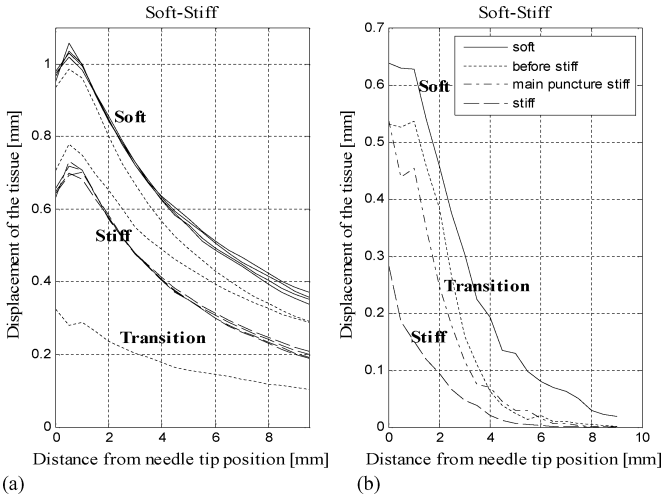

Fig. 9. Tissue displacement results upon needle insertion into a two-layer phantom: (a) simulation and (b) experiment.

different stiffnesses was distinguishable by the degree of tissue displacement, with increased displacement within the soft layer when compared to the stiff layer [see Fig. 9(a)]. Tissue displacement decreased upon needle insertion within the transition phase separating the two layers. An identical simulation was repeated for an inverted phantom model and yielded similar results.

d) Two layers—experiments: Results were also experimentally verified by a straight-line path needle insertion into a two-layer phantom. As seen in the simulation model, tissue displacements in the soft layers were larger than in the stiff layer and transition region [see Fig. 9(b)]. However, large displacements were observed when the needle was first inserted into the stiff material, seemingly due to the main puncture event that causes tissue advancement at the needle velocity until the puncture is completed [27]. Although the displacement at the transition and main puncture event phases are similar, they can be distinguished by the measured forces, where initial forces are highest when beginning insertion within the stiff layer. Tissue displacements recorded for the inverted phantom yielded similar results.

e) Tissue stiffness classification method—conclusion: The correlation between tissue stiffness and needle-induced tissue displacement was determined and verified by simulatory and experimental models. The results demonstrated enhanced tissue displacement in soft materials when compared to stiff materials. In addition, layer stiffness can be distinguished by the degree of tissue displacement upon needle insertion. However, in order to further quantify this correlation for any given tissue stiffness, additional measurements and calibrations are required to create a more complete stiffness versus displacement conversion table.

This method can be further employed to indicate when a needle tip reaches a target tissue of suspicious pathology affecting its stiffness.

E. Controlled Needle Insertion

Needle-tip tracking error can be minimized by the control-loop algorithm, as shown in Fig. 10, where the needle tip location, with no reference to its orientation, constitutes the input signal for the system.

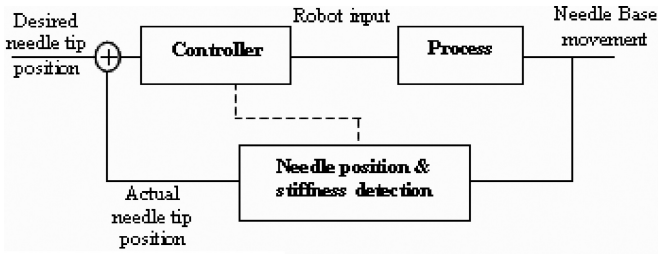

Fig. 10. Control-loop diagram.

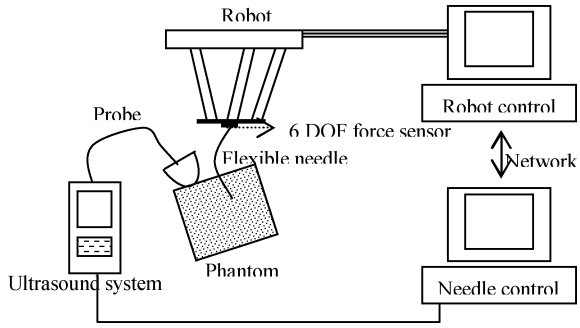

Fig. 11. Experimental setup.

The actual needle tip location, as derived from the ultrasound image, and its deviation from the planned path is then fed to the controller. The controller calculates the required needle base movement based on the inverse kinematics of the virtual spring model and also optimizes needle orientation to minimize lateral tissue pressure. The dashed line transfers the parameters pertaining to the detected tissue type and its stiffness to the controller.

III. Experimental Results

Needle-steering performance with open-loop, closed-loop, and closed-loop with updated tissue stiffness systems was measured by means of needle deviation from the desired path and precision at reaching the target.

A. Instrumentation

The experimental setup (see Fig. 11) included a Sonosite 180plus portable ultrasound system with a C60 curved imaging probe. A DFG/1394-1e video-to-FireWire converter (Imaging Source Europe) image transfer to the needle control computer for processing. The needle was connected to the revolute, spherical, prismatic, revolute (RSPR) 6-DOF parallel robot moving plate by an ATI Nano17 6-DOF force/torque sensor, which measured needle insertion forces and torques. A secondary computer controlled the robot, while a main computer was used for needle base movements calculation, needle and tissue stiffness classification, and needle control. The commands for robot motion were sent to the secondary computer via a local network. A Micro Scribe digitizer was used for the registration procedure. A stainless steel 20-gauge needle with a beveled tip was used in

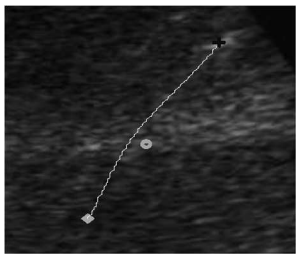

Fig. 12. Planned trajectory calculated by interpolation methods using the tip, target, and obstacle positions as key parameters.

all experiments. A two-layer dermasol phantom prepared with TiO2 and placed in a plastic container was used in the experimental setups. The virtual spring coefficients required for the needle-steering model were estimated for soft and stiff dermasol before beginning the experiment by laterally moving the needle inside the phantom and measuring the resulting force and needle tip deflection as previously described [14]. The calculated coefficients were 9 N/m and 23 N/m for soft and stiff dermasol, respectively. In addition, the ultrasound system accuracy was measured by comparing physical distances of a jig to those detected by the ultrasound probe. The mean error value was 1.23 with a standard deviation of 0.87 mm.

B. Typical Procedure

A typical needle insertion procedure involves placement of the ultrasound probe within the needle plane followed by performance of a registration procedure. After selecting the desired target on the image, a suggested needle entry point is computed according to the intersection point of a straight line passing through the target with inclination of the needle and the edge of the image. Obstacles between the target and the entry point are then outlined by the user. The robot is then programmed to move the needle to the entry point, and the algorithm for tip detection is applied to detect the initial position of the tip. A trajectory is then calculated by interpolation methods (spline method) based on the detected tip and target and obstacle positions. A typical trajectory of 35–40 mm in length and amplitude of about 2–3 mm was used in these experiments (see Fig. 12). The controlled needle insertion procedure could then be performed as described in Section II-E.

C. Experimental Results

Soft dermasol spring coefficient values were considered in both open- and closed-loop systems. More advanced closed-loop experiments considered tissue stiffness and updated the system accordingly throughout the insertion procedure. Fig. 13 presents the *x*-axis and *y*-axis tracking errors as a function of needle insertion depth and summarizes the mean and std errors for all experiments. While the resulting error for closed-loop systems was smaller than the open-loop systems, the closed-loop setup updated with tissue stiffness coefficients demonstrated the highest performance and accuracy with a maximum tracking error of about 1 mm. An image of the needle tip reaching the target in a closed-loop system with updated coefficient is shown

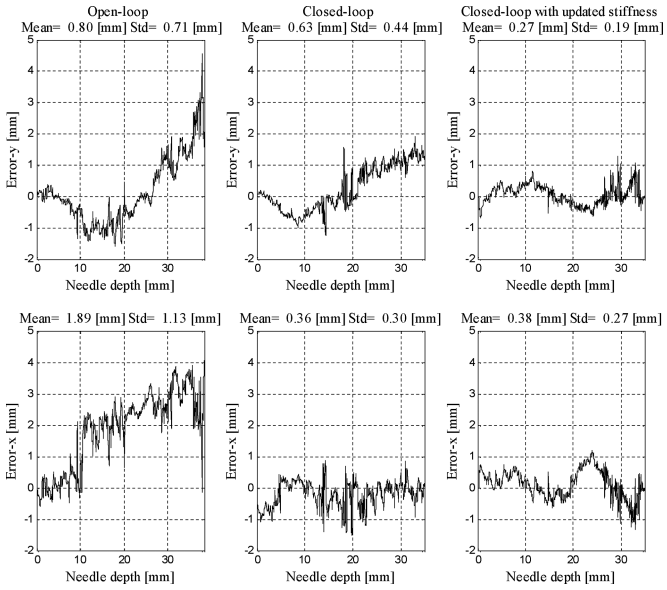

Fig. 13. Experimental results of needle-tip tracking error.

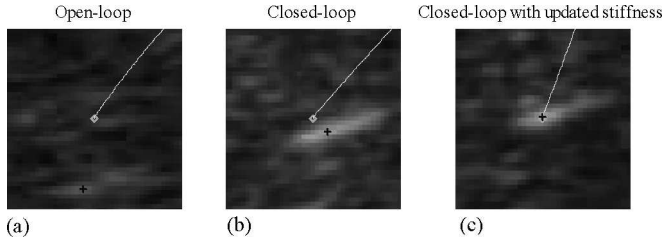

Fig. 14. Needle tip position at the last imaging frames of an (a) open loop, (b) closed loop, or a (c) closed loop with updated stiffness steering system.

in Fig. 14(c). The high positional accuracy is clearly evident and surpasses the 6–8 mm error range of the freehand needle insertion technique [6].

IV. Discussion and Conclusion

This paper describes the development of a robotic system for flexible needle steering under real-time ultrasound imaging. A 6-DOF robot is used to steer the needle along a curved trajectory by maneuvering the needle base. The needle tip position is continuously detected by an ultrasound sensor, and the tracking error constitutes the input to the controller, which then solves the inverse kinematics based on needle position and needle and tissue properties. The control algorithm is further improved by introducing a novel method to determine tissue properties based on tissue motion in response to needle tip insertion. This method was proven to successfully distinguish between soft and stiff tissues and could be further expanded to constitute a more complete and accurate correlation between tissue displacement and stiffness.

Experimental results of the closed-loop control system with updated tissue stiffness parameters demonstrated the best performance with a maximal needle-tip tracking error of 1 mm. The proposed system enables accurate maneuvering of a flexible needle along an optimized path while ensuring minimal

lateral needle displacement and minimal pressure on the tissue. The system offers an up to sixfold higher degree of accuracy than that reported freehand insertion techniques. Moreover, the ultrasound imaging modality provides significant advantages over other imaging methods by avoiding hazardous radiation, cutting costs, and increasing high accessibility and portability.

Future work will expand the described model and imaging method to include sensitivity toward 3-D parameters, enabling control out-of-plane needle motion and improved needle visibility. Furthermore, a theoretical model will be developed to determine the correlation between tissue displacement and tissue stiffness.

REFERENCES

[1] S. Nath, Z. Chen, N. Yue, S. Trumpore, and R. Peschel, "Dosimetric effects of needle divergence in prostate seed implant using 125I and 103Pd radioactive seeds," *Med. Phys.*, vol. 27, no. 5, pp. 1058–1066, May 2000.

[2] J. Greif, O. Merimsky, S. Marmur, A. N. Staroselsky, and Y. Schwarz, "Correlative study of preoperative transthoracic core cutting needle biopsy of focal thoracic lesions and thoracotomy findings," *Acta Oncologica*, vol. 39, no. 4, pp. 491–493, Oct. 2000.

[3] G. Megali, O. Tonet, C. Stefanini, M. Boccadoro, V. Papaspyropoulos, L. Angelini, and P. Dario, "A computer-assisted robotic ultrasound-guided biopsy system for video-assisted surgery," in *Proc. Med. Image Comput. Comput.-Assisted Intervention*, 2001, pp. 343–350.

[4] K. J. Surry, W. L. Smith, L. J. Campbell, G. R. Mills, D. B. Downey, and A. Fenster, "The development and evaluation of a three-dimensional ultrasound-guided breast biopsy apparatus," *Med. Image Anal.*, vol. 6, pp. 301–312, Sep. 2002.

[5] A. Melzer, B. Gutmann, T. Remmele, R. Wolf, A. Lukoscheck, M. Bock, H. Bardenheuer, and H. Fischer, "Innomotion for percutaneous image-guided interventions," *IEEE Eng. Med. Biol. Mag.*, vol. 27, no. 3, pp. 66–73, Jun. 2008.

[6] E. M. Boctor, M. A. Choti, E. C. Burdette, and R. J. Webster, "Three-dimensional ultrasound-guided robotic needle placement: An experimental evaluation," *Int. J. Med. Robot. Comput. Assist. Surg.*, vol. 4, pp. 180–191, Apr. 2008.

[7] D. Stoianovici, K. Cleary, A. Patriciu, D. Mazilu, A. Stanimir, N. Craciunoiu, V. Watson, and L. Kavoussi, "AcuBot: A robot for radiological interventions," *IEEE Robot. Autom. Mag.*, vol. 19, no. 5, pp. 927–930, Oct. 2003.

[8] K. Cleary, A. Melzer, V. Watson, G. Kronreif, and D. Stoianovici, "Interventional robotic systems: applications and technology state-of-the-art," *Minim. Invasive. Ther. Allied Technol.*, vol. 15, no. 2, pp. 101–113, 2006.

[9] S. P. DiMaio and S. E. Salcudean, "Needle insertion modeling and simulation," in *Proc. IEEE Int. Conf. Robot. Autom.*, May 2002, pp. 2098–2105.

[10] R. Alterovitz, J. Pouliot, R. Taschereau, I.-C. J. Hsu, and K. Goldberg, "Simulating needle insertion and radioactive seed implantation for prostate brachytherapy," in *Medicine Meets Virtual Reality*, vol. 11, J. D. Westwood *et al.*, Eds. Amsterdam, The Netherlands: IOS Press, Jan. 2003, pp. 19–25.

[11] C. Simone and A. M. Okamura, "Modeling of needle insertion forces for robot-assisted percutaneous therapy," in *Proc. IEEE Int. Conf. Robot. Autom.*, May 2002, pp. 2085–2091.

[12] S. P. DiMaio and S. E. Salcudean, "Needle steering and model-based trajectory planning," in *Proc. Med. Image Comput. Comput.-Assisted Intervention* (Lecture Notes in Computer Science), Montreal, QC, Canada, 2003, vol. 2878, pp. 33–40.

[13] R. Alterovitz and K. Goldberg, "Planning for steerable bevel-tip needle insertion through 2D soft tissue with obstacles," in *Proc. IEEE Int. Conf. Robot. Autom.*, Barcelona, Spain, Apr. 2005, pp. 1640–1645.

[14] D. Glozman and M. Shoham, "Flexible needle steering and optimal trajectory planning for percutaneous therapies," in *Proc. Med. Image Comput. Comput.-Assisted Intervention*, Saint-Malo, France, Sep. 2004, pp. 137–144.

[15] I. Schafhalter-Zoppoth, C. E. McCulloch, and A. T. Gray, "Ultrasound visibility of needles used for regional nerve block: An *in vitro* study," *Reg. Anesth Pain Med.*, vol. 29, no. 5, pp. 480–488, Oct. 2004.

[16] J. Hong, T. Dohi, M. Hashizume, K. Konishi, and N. Hata, "An ultrasound driven needle insertion robot for percutaneous cholecystostomy," *Phys. Med. Biol*, vol. 49, pp. 441–455, 2004.

[17] R. H. Gottlieb, W. B. Robinette, D. J. Rubens, D. F. Hartley, P. J. Fultz, and M. R. Violant, "Coating agent permits improved visualization of biopsy needles during sonography," *Amer. J. Roentgenology*, vol. 171, pp. 1301–1302, Nov. 1998.

[18] R. A. Beasley, J. D. Stefansic, A. J. Herline, L. Guttierez, and R. L. Galloway, Jr., "Registration of ultrasound images," *Proc. SPIE*, vol. 3658, pp. 125–132, May 1999.

[19] J. Ophir, S. K. Alam, B. S. Garra, F. Kallel, E. E. Konofagou, T. Krouskop, C. R. B. Merritt, R. Righetti, R. Souchon, S. Srinivasan, and T. Varghese, "Elastography: Imaging the elastic properties of soft tissues with ultrasound," *J. Med. Ultrason.*, vol. 29, pp. 155–171, 2002.

[20] F. Yeung, S. F. Levinson, and K. J. Parker, "Multilevel and motion model-based ultrasonic speckle tracking algorithms," *Ultrasound Med. Biol.*, vol. 24, pp. 427–441, 1998.

[21] A. Basarab, H. Liebgott, F. Morestin, A. Lyshchik, T. Higashi, R. Asato, and P. Delachartre, "A method for vector displacement estimation with ultrasound imaging and its application for thyroid nodular disease," *Med. Image Anal.*, vol. 12, pp. 259–274, Oct. 2007.

[22] E. Dehghan, X. Wen, R. Zahiri-Azar, M. Marchal, and S. E. Salcudean, "Needle–tissue interaction modeling using ultrasound-based motion estimation: Phantom study," Comput. Aided Surg., vol. 13, no. 5, pp. 265–280, Sep. 2008.

[23] J. A. Jensen, "Field: A program for simulating ultrasound systems," in *Proc. 10th Nordic-Baltic Conf. Biomed. Imag. Published Med. Biol. Eng. Comput.*, vol. 34, pp. 351–353, 1996.

[24] J. A. Jensen and N. B. Svendsen, "Calculation of pressure fields from arbitrarily shaped, apodized, and excited ultrasound transducers," *IEEE Trans. Ultrason., Ferroelectr., Freq. Control*, vol. 39, no. 2, pp. 262–267, Mar. 1992.

[25] [Online]. Available: http://server.oersted.dtu.dk/personal/jaj/field/

[26] [Online]. Available: http://www.cal-med-innovations.com/dermasol.html

[27] J. T. Hing, A. D. Brooks, and J. P. Desai, "Reality-based needle insertion simulation for haptic feedback in prostate brachytherapy," in *Proc. IEEE Int. Conf. Robot. Autom.*, May 2006, pp. 619–624.

Zipi Neubach received the B.Sc. degree in biomedical engineering, in 2003, from the Technion-Israel Institute of Technology, Haifa, Israel, where she is currently working toward the M.Sc. degree at the Robotics Laboratory, Mechanical Engineering Department.

From 2003 to 2006, she was a System Engineer at the General Electric Ultrasound Israel, Tirat-Hacarmel, Israel. She qualified in medical imaging and biotechnology from the Technion-Israel Institute of Technology. Her research interests include medical robotics, medical imaging, and medical devices.

Moshe Shoham (A'89) received the B.Sc., M.Sc., and D.Sc. degrees from Technion–Israel Institute of Technology, Haifa, Israel.

He has been conducting research in robotics for the past 25 years, with a special focus on new robot structures and on medical applications. He has been the Head of the Robotics Laboratory, Mechanical Engineering Department, Columbia University, New York, and Robotics Laboratory, Mechanical Engineering Department, Technion-Israel Institute of Technologies. In 2001, he founded Mazor Surgical Technologies. His research activity has been funded by the grants from commercial companies as well as governmental agencies in Israel, United States, French, Italy, and the EC. He is the author or coauthor of more than 150 conference and journal papers and two books.

Prof. Shoham has served as a Technical Editor for the IEEE TRANSACTIONS ON ROBOTICS AND AUTOMATION. He is a Fellow of the American Society of Mechanical Engineers.